

Hierarchical multiscale hyperporous block copolymer membranes via tunable dual-phase separation

Seungmin Yoo,* Jung-Hwan Kim,* Myoungsoo Shin, Hyungmin Park, Jeong-Hoon Kim, Sang-Young Lee,[†] Soojin Park[†]

2015 © The Authors, some rights reserved; exclusive licensee American Association for the Advancement of Science. Distributed under a Creative Commons Attribution NonCommercial License 4.0 (CC BY-NC). 10.1126/sciadv.1500101

The rational design and realization of revolutionary porous structures have been long-standing challenges in membrane science. We demonstrate a new class of amphiphilic polystyrene-*block*-poly(4-vinylpyridine) block copolymer (BCP)-based porous membranes featuring hierarchical multiscale hyperporous structures. The introduction of surface energy-modifying agents and the control of major phase separation parameters (such as nonsolvent polarity and solvent drying time) enable tunable dual-phase separation of BCPs, eventually leading to macro/nanoscale porous structures and chemical functionalities far beyond those accessible with conventional approaches. Application of this BCP membrane to a lithium-ion battery separator affords exceptional improvement in electrochemical performance. The dual-phase separation-driven macro/nanopore construction strategy, owing to its simplicity and tunability, is expected to be readily applicable to a rich variety of membrane fields including molecular separation, water purification, and energy-related devices.

INTRODUCTION

Porous membranes have attracted considerable attention in various industrial fields including water purification, bioseparation, chemical sensing, and energy storage (1–6). Synthetic porous membranes are typically fabricated by sintering of organic and/or inorganic materials, stretching of polymer films, ion track etching, template leaching, and phase inversion (7–9). Among the various building blocks for use in porous membranes, block copolymers (BCPs) have been extensively investigated because of their self-assembly-enabled nanodomains (10–12). Through spinodal decomposition, breath figures, solvent swelling, and nonsolvent-induced phase separation (NIPS), BCPs can produce precisely defined porous structures in versatile shapes (13–24).

For membrane fabrication, NIPS (or immersion precipitation) has been of great interest because of its simplicity and scalability. In NIPS, the morphologies of the resulting membranes can be adjusted by combining phase separation thermodynamics with mass transport phenomena (9). For membrane-driven purification and separation processes, an asymmetric porous structure is preferable because it endows the membranes with selectivity and permeability. Asymmetric structures with well-organized skin layers have been explored using self-assembled BCP films (13). Upon immersion of BCP solutions into a nonsolvent, the time-controlled evaporation of a volatile solvent produces a skin layer with a vertically aligned cylindrical structure supported by a graded porous layer. Porous membranes with symmetric structures are suitable for two-way ion transport, an essential prerequisite for separator membranes in rechargeable power sources. The macropore size of NIPS-based BCP membranes is determined by polymer concentrations and solvent-nonsolvent exchange kinetics, whereas the nanopore size depends on the compatibility between the pore-forming block and the nonsolvent. Conventional NIPS-based BCP membranes, however, tend to have poorly developed nanopores mainly because of

the limited compatibility between the pore-forming block and the nonsolvent (16). To date, the most common way to tune nanoporous structure has been limited to varying the molecular weight and chemical composition of the pore-forming blocks, the blending of BCPs, and the postprocessing treatment (that is, atomic layer deposition and molecular vapor deposition) of BCPs (16, 22–25).

Here, as a new strategy to address these challenging issues, we demonstrate new surface energy-tailored amphiphilic polystyrene-*block*-poly(4-vinylpyridine) (PS-*b*-P4VP) BCP membranes with hierarchical multiscale hyperporous structures (referred to as “HMH-BCP membranes”) and chemical functionality. The introduction of a surface energy-modifying agent into a pore-forming block of an amphiphilic BCP via nucleophilic substitution, along with finely controlling the nonsolvent polarity and solvent drying time, enables the tunable dual-phase separation of BCPs, leading to a hierarchical macro/nanoscale porous structure and chemical functionality far beyond those achievable with conventional membrane technologies.

RESULTS

Fabrication of HMH-BCP membrane with hierarchical multiscale structure

Figure 1 depicts the fabrication and physical appearance of the HMH-BCP membrane, along with the nucleophilic substitution reaction of the amphiphilic PS-*b*-P4VP BCP with the surface energy-modifying agent 3-glycidoxypropyltrimethoxysilane (GPTMS). The chemical reaction between the pyridine moiety of the P4VP block and the epoxide of the GPTMS (26) creates a new cyclic amide-bearing compound (denoted as PS-*b*-G-P4VP). The reaction was initiated by nucleophilic attack of the nitrogen atoms of P4VP on the epoxide groups of GPTMS. Immediately after the nucleophilic attack, the oxygen anion of the epoxide groups attacks the α -position carbon of pyridine rings. As a consequence, the aromatic structure of pyridine ring is destroyed, resulting in the formation of the six-membered rings bearing the conjugated 3,5-dienes. Then, the conjugated 3,5-dienes could undergo

Department of Energy Engineering, School of Energy and Chemical Engineering, Ulsan National Institute of Science and Technology (UNIST), UNIST-gil 50, Ulsan 689-798, Republic of Korea.

*These authors contributed equally to this work.

[†]Corresponding author. E-mail: spark@unist.ac.kr (S.P.); syleek@unist.ac.kr (S.-Y.L.)

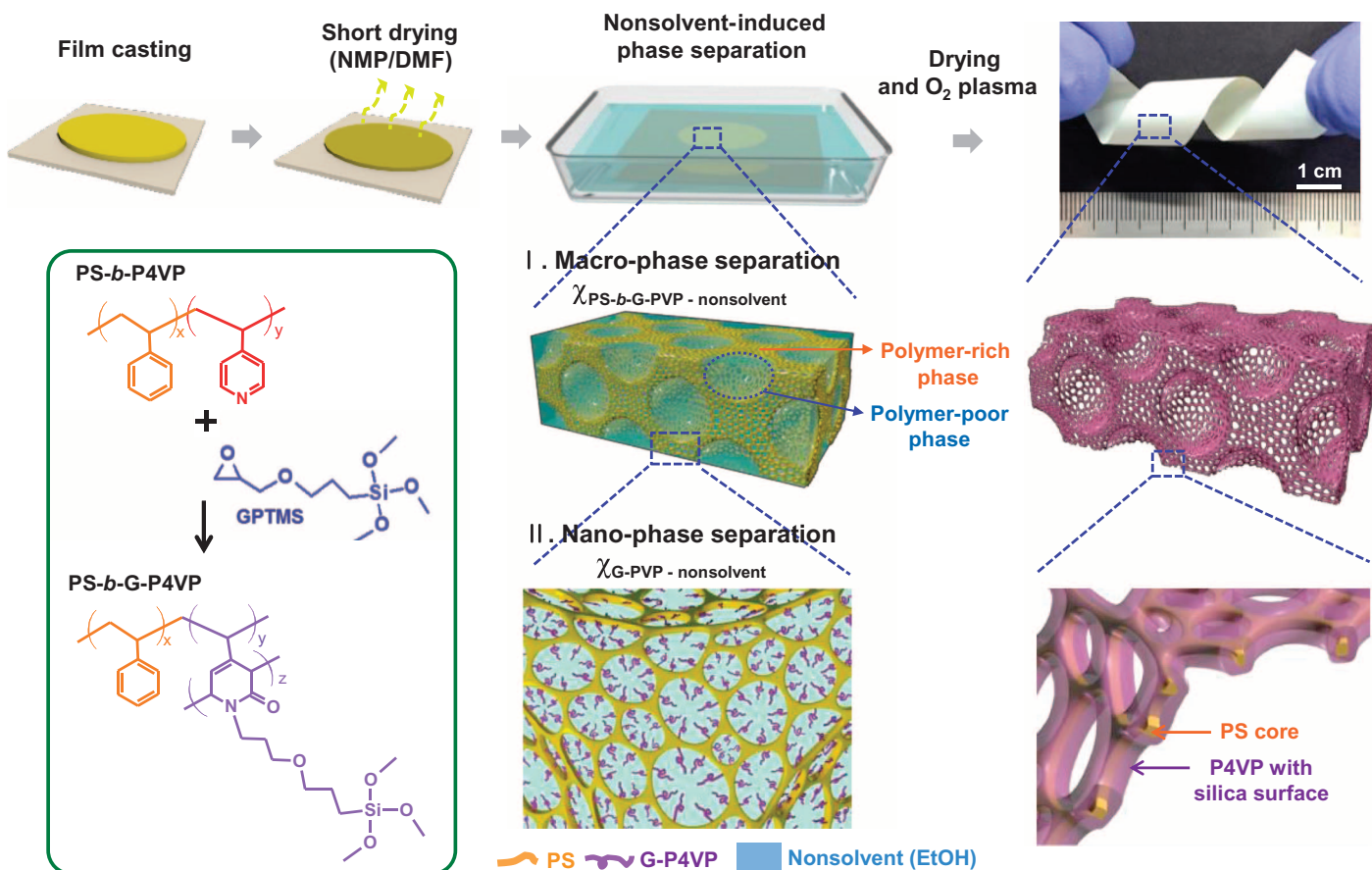


Fig. 1. Schematic illustration showing the fabrication and physical appearance of HMH-BCP membranes. Bottom left: Nucleophilic substitution reaction between the pyridine moiety of the PS-*b*-P4VP and the surface energy-modifying agent GPTMS to generate PS-*b*-G-P4VP. Subsequent solvent-nonsolvent exchange leads to macro/nano-phase separation to form the hierarchical multiscale hyperporous structure.

Diels-Alder reaction at elevated temperature (120°C) and subsequent rearrangement to form a cyclic amide (fig. S1). The relatively hydrophobic nature of GPTMS renders the resulting alkylated P4VP block hydrophobic. Note that the solubility parameters of P4VP and GPTMS are 22.2 and 7.08 MPa^{1/2}, respectively (20, 27). This PS-*b*-G-P4VP solution is cast on copper foil and the solvent [*N*-methyl-2-pyrrolidone/dimethylformamide (NMP/DMF), 80:20 (v/v)] is quickly evaporated to acquire a more concentrated polymer solution. During drying, the high thermal conductivity of the copper substrate allows faster solvent evaporation as well as a uniform distribution of the BCP throughout the whole thickness direction. Subsequently, the incompletely dried BCP mixture is immersed into a coagulation bath containing ethanol (as a nonsolvent), leading to a porous solid-state film via NIPS. Ethanol, miscible with the NMP/DMF solvent mixture, is a relatively favorable solvent for the bare PS-*b*-P4VP but is a poor solvent for the PS-*b*-G-P4VP because of the presence of the hydrophobic GPTMS groups. Upon solvent-nonsolvent exchange, a macro-phase separation occurs to afford a macroporous scaffold structure consisting of BCP-rich and BCP-poor phases. Simultaneously, the BCP-rich phase undergoes a nano-phase separation because of the self-assembling nature of the BCP, which generates a quasi-hexagonally packed structure composed of the PS and G-P4VP blocks (holding a small amount of nonsolvent). Complete drying of the nonsolvent gives an HMH-BCP membrane featuring a hierarchical multiscale (macro/nano) hyperpo-

rous structure. Intriguingly, the pore surface of the HMH-BCP membrane is preferentially covered with G-P4VP blocks. Finally, oxygen plasma treatment is performed to remove dense BCP layers from the top and bottom surfaces and to transform the organic Si-containing G-P4VP blocks into inorganic silica layers, which contribute to the chemical resistance and thermal stability of the HMH-BCP membrane. The fabrication of membrane without any large-scale defects is essential for final membrane applications. The typical area of the membrane was 10 cm × 20 cm, which could be further adjusted by varying the dimensions of the doctor blade. To get a high-quality membrane, controlling dry time before putting a precursor polymer solution into a coagulation bath is critical. Short dry time may give rise to formation of some large pinholes, whereas long dry time would not guarantee a well-developed dual-porous structure because of the lack of remaining solvent. More details on the fabrication of PS-*b*-G-P4VP membranes are given in Materials and Methods.

Cross-sectional scanning electron microscopy (SEM) images show that the HMH-BCP membrane has a highly ordered hierarchical multiscale structure with a dual-porous structure (Fig. 2, A and B). More notably, the dual-porous structure is uniformly distributed over the entire thickness direction (Fig. 2, C and D). The effect of oxygen plasma treatment on the porous morphology of the HMH-BCP membrane was also examined (fig. S2). The anomalous dual-porous structure was quantitatively analyzed in great detail using mercury intrusion

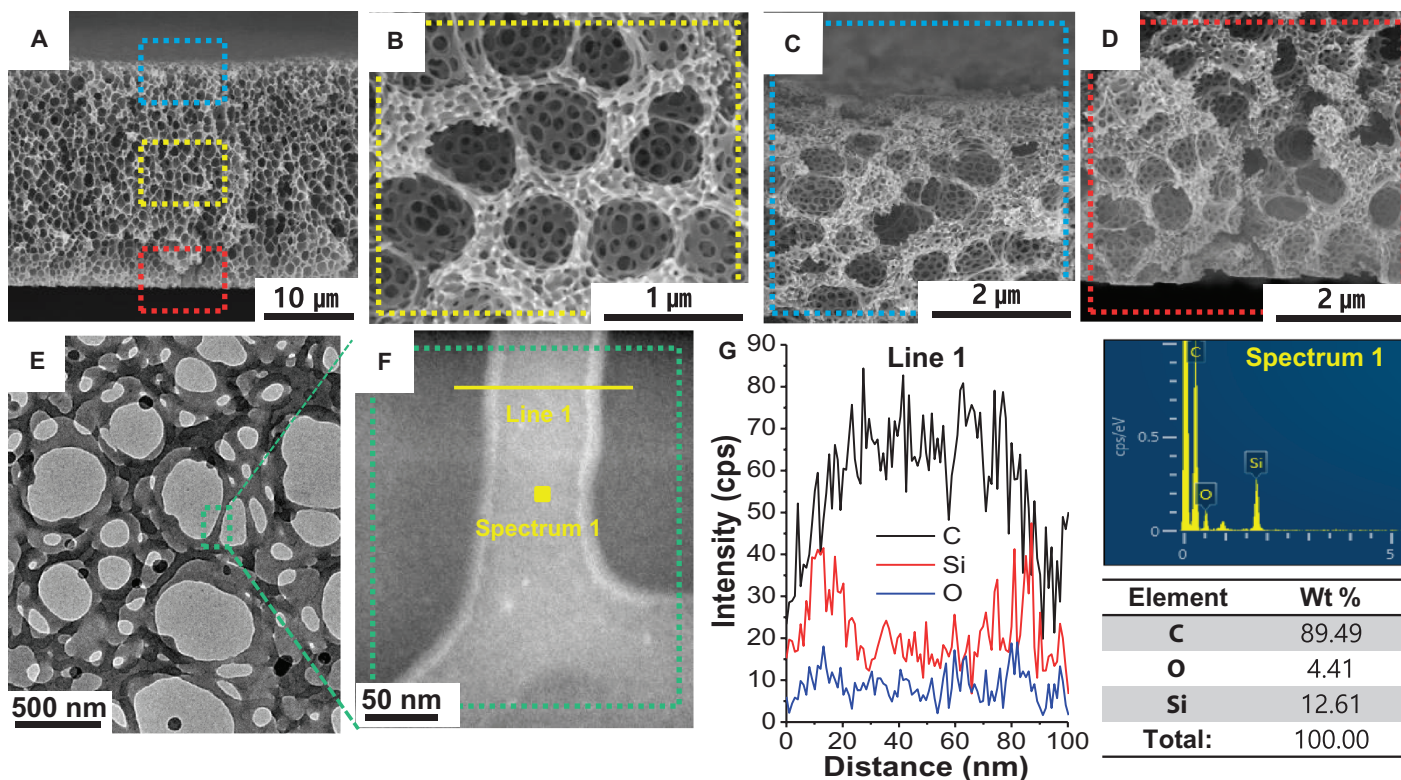


Fig. 2. Structural uniqueness of HMH-BCP membranes. (A to D) Cross-sectional SEM images showing hyperporous membranes with micro- and nanopores over the entire film thickness direction. (B to D) Magnified images of the rectangular boxes shown in (A). (E) TEM image of an HMH-BCP thin film fabricated from 1 wt % PS-*b*-G-P4VP solution. (F) HAADF-STEM image taken from the green box shown in (E). (G) EDS line-scan profile and point spectrum taken from the yellow line and point in the STEM image shown in (F). cps, counts per second.

porosimetry (fig. S3), exhibiting average pore sizes of ~ 1300 nm (for macropores) and ~ 160 nm (for nanopores).

For detailed information on the HMH-BCP membrane, as a model experiment, a thin porous membrane was fabricated on a copper grid using 1 weight percent (wt %) PS-*b*-G-P4VP solution via the same procedure described above. Figure 2E shows that the thin membrane has a porous structure that appears similar to that of the HMH-BCP membrane (Fig. 2, A and B). A high-angle annular dark-field scanning transmission electron microscopy (HAADF-STEM) image (Fig. 2F) and energy-dispersive x-ray spectroscopy (EDS) analysis (Fig. 2G) reveal that the entire surface of the thin membrane is covered with G-P4VP blocks. To examine the internal morphology of the HMH-BCP membrane, the membrane was sliced to a nominal thickness of 100 nm using an ultramicrotome. The TEM and EDS mapping images show that the entire surface of the membrane is covered with silica layers (fig. S4). Furthermore, surface depth profiling by time-of-flight secondary ion mass spectrometry (TOF-SIMS) indicates that the nitrogen content of the pyridine in the P4VP block tends to increase with etching depth (fig. S5).

These structural characterization results demonstrate that the G-P4VP block has a stronger affinity for the nonsolvent (ethanol) than the PS block. Consequently, the PS-*b*-G-P4VP undergoes dual-phase separation, yielding multiscale hyperporous structures. The unusual dual-phase separation occurs only when BCPs fulfill the following prerequisites: they are immiscible with the nonsolvent overall, but one of the blocks must be partially miscible with the nonsolvent. To support this hypothesis, a control BCP membrane was fabricated using bare PS-*b*-P4VP. Com-

pared to the PS-*b*-G-P4VP, the nonalkylated BCP produced a sponge-like structure because ethanol is a good solvent for the P4VP block (fig. S6). This result confirms that the surface energy-modifying agent (here, GPTMS) plays a viable role in enabling the dual-phase separation.

To explore the versatility of the HMH-BCP membrane strategy, polystyrene-*block*-poly(2-vinylpyridine) (PS-*b*-P2VP) was chosen and subjected to the substitution reaction with GPTMS. PS-*b*-G-P2VP was obtained despite the lower reactivity of the starting material compared with P4VP (fig. S7) (25). Similar to PS-*b*-G-P4VP, the PS-*b*-G-P2VP membrane exhibited a well-defined multiscale hyperporous structure (fig. S8).

Effects of phase separation variables on structural evolution of HMH-BCP membranes

The effect of the extent of GPTMS substitution on the morphology of the PS-*b*-G-P4VP membrane was investigated in more detail by varying the substitution reaction time from 10 to 120 min. Initially, the sponge-like structure, which is commonly observed in typical BCPs (20, 22), is formed (Fig. 3, A and E). A trace of the dual-porous structure is found in the membrane at a reaction time of 20 min (fig. S9). Notably, at 30 min, a well-developed hierarchical multiscale hyperporous structure having macropores of ~ 800 nm and nanopores of ~ 120 nm is formed (Fig. 3, B and F). Further increases in the reaction time result in reduced nanopore size (an average pore diameter of 70 nm) (Fig. 3C), resulting in closed pores (Fig. 3, D and H) because of the GPTMS-driven hydrophobicity change. The GPTMS content of PS-*b*-G-P4VP, which was estimated from the analysis of silicon atoms, tends to gradually increase with reaction

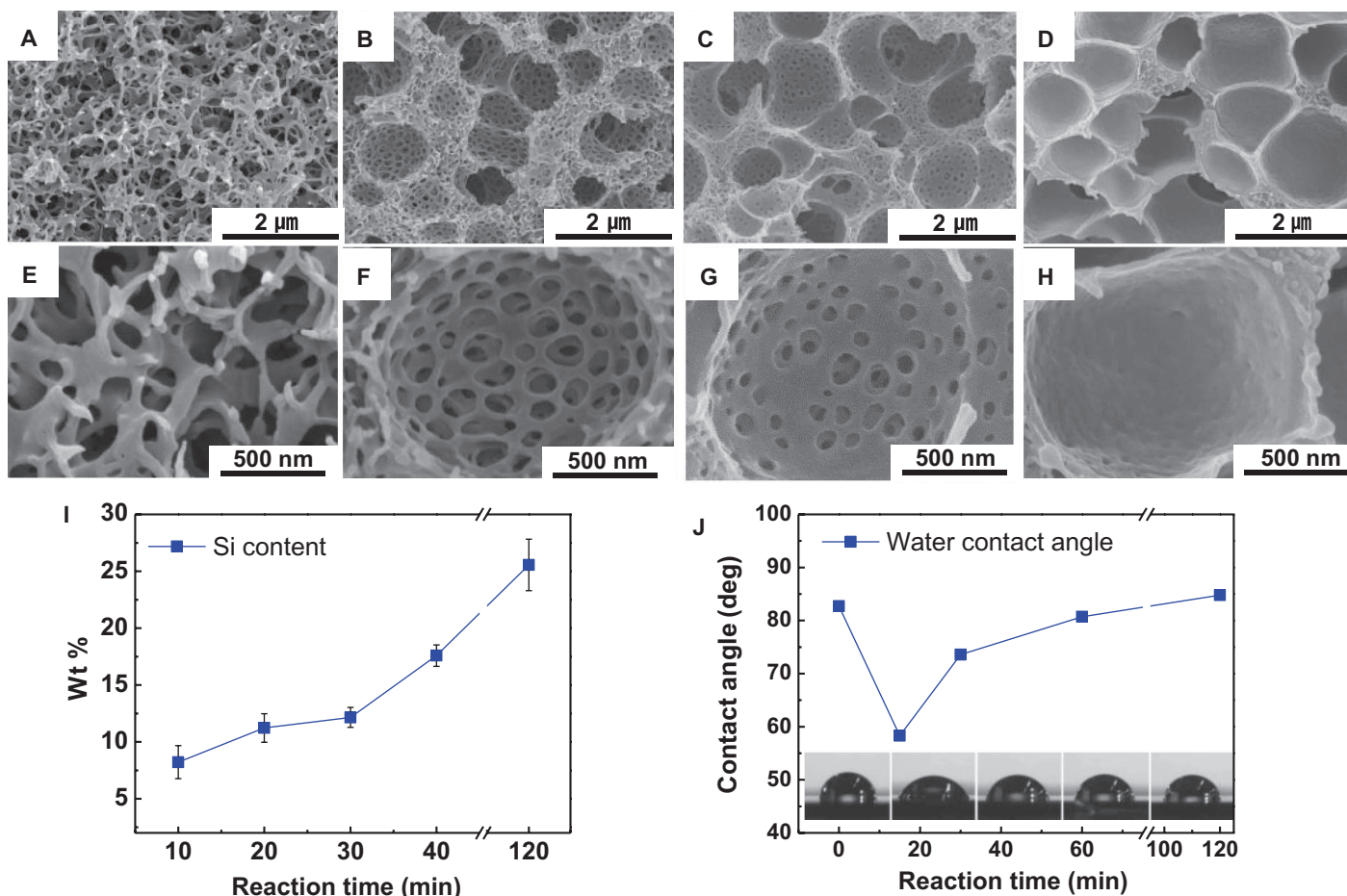


Fig. 3. Effect of GPTMS content (determined by the reaction time) on morphology (cross-sectional SEM image) of PS-*b*-G-P4VP membranes. (A to D) GPTMS substitution reaction time: (A) 0 min (bare PS-*b*-P4VP), (B) 30 min, (C) 40 min, and (D) 120 min. (E to H) Magnified views of the SEM images shown in (A) to (D). (I) Change in Si content (corresponding to GPTMS) of PS-*b*-G-P4VP with GPTMS substitution reaction time. (J) Change in water contact angle of PS-*b*-G-P4VP thin films with GPTMS substitution reaction time.

time (Fig. 3I). This result was further confirmed by measuring the water contact angles of PS-*b*-G-P4VP thin films having different GPTMS contents (Fig. 3J). A bare PS-*b*-P4VP BCP (that is, before being modified with GPTMS) is hydrophobic. When we selectively introduced GPTMS to the P4VP block of the PS-*b*-P4VP BCP, the resulting GPTMS-modified P4VP block started to show hydrophilicity due to the formation of cyclic amide bonding. Further incorporation of GPTMS, however, leads to increasing the concentration of hydrophobic siloxane groups (originating from GPTMS), rendering the GPTMS-modified P4VP block hydrophobic. Eventually, the GPTMS-modified P4VP block tends to gradually become more hydrophobic with increasing GPTMS content. Such intriguing morphological changes with substitution reaction time can be explained by considering a ternary phase diagram (fig. S10).

In addition to the degree of GPTMS substitution, a change in the nonsolvent (in terms of hydrophilicity) in the coagulation bath exerts a significant influence on the nanoporous structure of the HMH-BCP membranes. Water, which is more hydrophilic than ethanol, was used as a nonsolvent. Relatively poorly developed, smaller nanopores were formed in the resulting membrane (fig. S11). The solvent drying time of BCP solutions (before being immersed into the nonsolvent), which affects the remaining solvent content in the PS-*b*-G-P4VP, was exam-

ined as another important variable in determining the porous morphologies of the BCP membranes (fig. S12).

Electrochemical test of the cells with HMH-BCP membrane

Stimulated by the hierarchical multiscale porous structure and higher porosity of the PS-*b*-G-P4VP membrane, we explored its potential as an alternative separator suitable for high-power lithium-ion batteries (LIBs). Porous separators in LIBs allow ion transport (after being filled with liquid electrolytes) between electrodes and prevent internal short-circuit problems (28). Here, a lithium titanium oxide ($\text{Li}_4\text{Ti}_5\text{O}_{12}$) anode and a lithium manganese oxide (LiMn_2O_4) cathode were chosen as a model electrode system to evaluate the electrochemical performance of cells containing the HMH-BCP membrane (thickness, 25 μm ; porosity, ~70%) (fig. S3), where the mass loadings of the electrodes were 24.5 and 18.5 mg cm^{-2} , respectively. As a control separator, a commercially available polypropylene (PP)/polyethylene (PE)/polypropylene (PP) separator (Celgard; thickness, 20 μm ; porosity, ~40%) was used. The cell with the HMH-BCP membrane showed normal charge/discharge behavior at low current density (fig. S13A), similar to the cell incorporating the PP/PE/PP separator. The HMH-BCP membrane exhibited superior rate capability (discharge capacity ratio, 76.6% at 2.0 C/0.5 C; charge capacity

ratio, 54.4% at 2.0 C/0.5 C) and cycle performance (capacity retention, 94.7% after 100 cycles at 1.0 C/1.0 C) at room temperature, in comparison to the PP/PE/PP separator (Fig. 4, A and B). These results demonstrate that the HMH-BCP membrane, owing to its precisely tuned, highly developed porous structure far beyond that accessible with commercial polyolefin separators, allows fast and uniform ionic flow between the cathode and anode, eventually alleviating porous separator-induced cell polarization during charge/discharge reactions (8). Such facile ion transport via the HMH-BCP membrane was further verified by the galvanostatic intermittent titration technique (GITT). During charging and discharging, the cell with the HMH-BCP membrane showed lower internal cell resistance than the one with the PP/PE/PP separator (fig. S13B).

LiMn₂O₄ cathodes suffer from serious loss of high-temperature cycling performance, mainly due to Mn dissolution, which increases with temperature (29–31). Figure 4C shows that the cell incorporating

the HMH-BCP membrane provided unprecedented improvement in the high-temperature (50°C) cycling performance (capacity retention, 92.0% after 200 cycles at 1 C/1 C), compared to the cell with the PP/PE/PP separator (capacity retention, 32.0% after 200 cycles at 1 C/1 C). To explain such exceptional cycling performance for the HMH-BCP membrane, we conducted an in-depth structural characterization of the separators after 200 cycles. The HMH-BCP membrane showed a high intensity of P–F stretching in the FTIR spectrum and larger amounts of P and F atoms in the EDS analysis (fig. S14). These results may be attributed to the strong electrostatic interactions between PF₆[−] and protonated pyridine or its derivatives (including unreacted pyridine, amide, and pyridone moieties) of the G-P4VP blocks (32). Moreover, TOF-SIMS analysis reveals that characteristic peaks of CF[−] and SiF[−] were newly observed in the HMH-BCP membrane, whereas the SiO[−] peak disappeared (Fig. 4D). By comparison, the PP/PE/PP separator

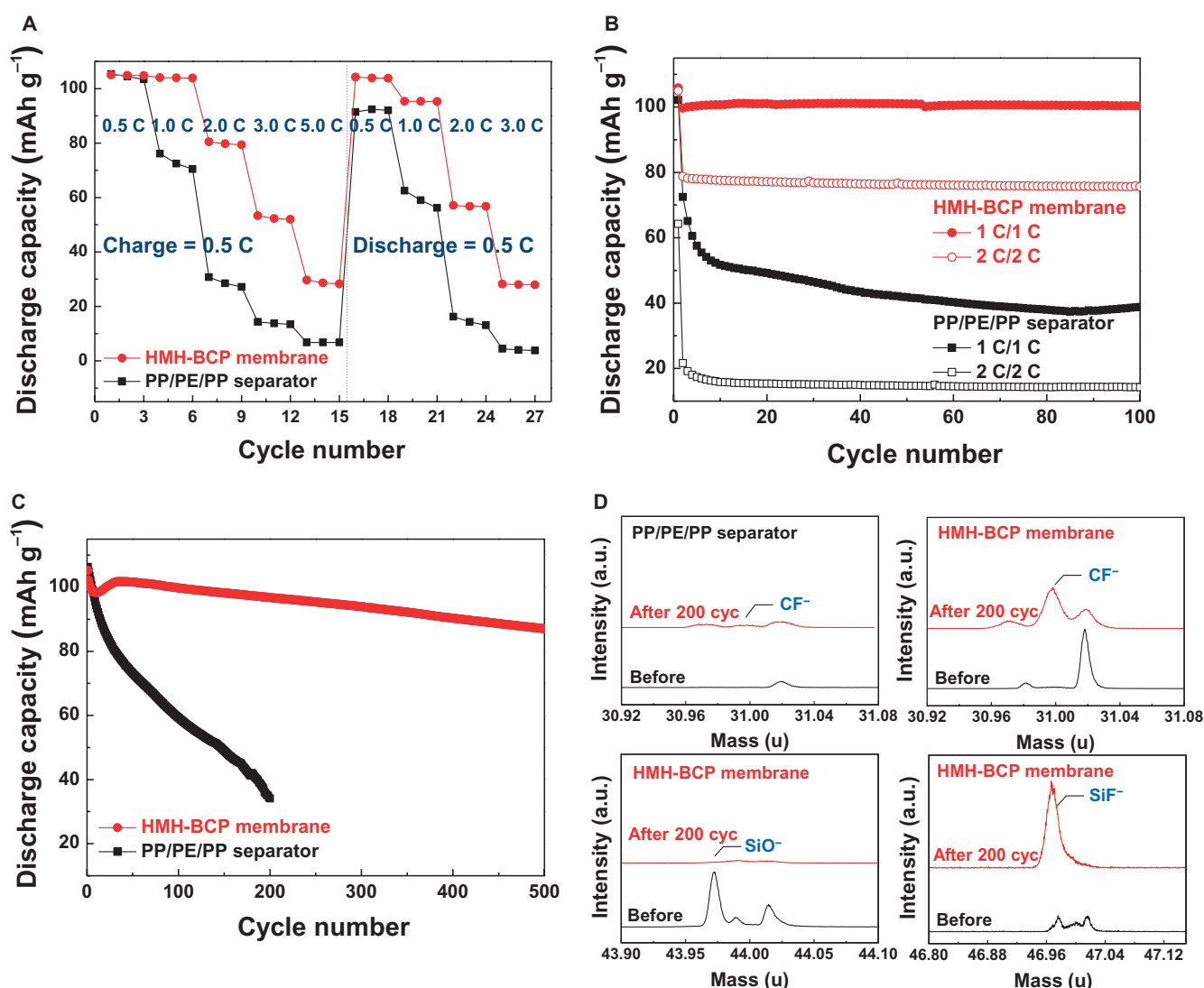


Fig. 4. Application of HMH-BCP membrane to a LIB separator versus a commercial PP/PE/PP separator as a control sample. (A) Charge/discharge rate capabilities of the HMH-BCP membrane [1st to 15th cycles: under a fixed charge current density (0.5 C) and various discharge current densities (0.5 to 5.0 C); 16th to 27th cycles: under a fixed discharge current density (0.5 C) and various charge current densities (0.5 to 3.0 C)]. **(B)** Cycling performance at high charge/discharge current densities (1.0/1.0 C, 2.0/2.0 C) at room temperature. **(C)** Long-term cycling performance (charge/discharge current density, 1.0/1.0 C) at 50°C. All cells were cycled in the voltage range of 1.5 to 2.8 V. **(D)** TOF-SIMS analysis of the separators before and after high-temperature cycling test (200 cycles). a.u., arbitrary units.

showed no CF^- peak. These results indicate that the G-P4VP block in the HMH-BCP membrane acts as a hydrofluoric acid (HF) scavenger, which, in turn, produces F-containing molecules incorporating CF^- and SiF^- (33). HF, which is mainly generated through side reactions between residual water molecules and the LiPF_6 -containing electrolyte (30), is a major cause of the unwanted Mn dissolution. Therefore, the HF scavenging capability of the HMH-BCP membrane is believed to exert a beneficial influence on the high-temperature cycling performance.

DISCUSSION

In summary, we fabricated an HMH-BCP membrane with a hierarchical multiscale (macro/nano) hyperporous structure via the dual-phase separation of the PS-*b*-G-P4VP BCP. GPTMS-mediated surface energy control of the PS-*b*-G-P4VP, with a particular focus on nanoscale phase separation between the G-P4VP block and the nonsolvent, played a critical role in enabling the remarkable achievement of a porous structure far beyond those accessible with conventional membrane technologies. The effects of nonsolvent polarity and solvent drying time on the dual-phase separation were also systematically investigated. As a proof of concept to verify the beneficial features of the HMH-BCP membrane, its application as a LIB separator was explored. The HMH-BCP separator membrane showed exceptional charge/discharge rate performance and high-temperature cycling performance. The HMH-BCP membrane, owing to its fabrication simplicity and compelling structural advantages, may be applicable in a wide range of membrane fields, and thus holds great promise as a new opportunity for unprecedented breakthroughs in membrane science and technology.

MATERIALS AND METHODS

Materials

PS-*b*-P4VP (number-average molecular weights $M_n^{\text{PS}} = 233$ kg/mol and $M_n^{\text{P4VP}} = 133$ kg/mol; dispersity M_w/M_n , 1.13; domain spacing, 90.93 nm) and PS-*b*-P2VP (number-average molecular weights $M_n^{\text{PS}} = 440$ kg/mol and $M_n^{\text{P2VP}} = 353$ kg/mol; dispersity M_w/M_n , 1.19) diblock copolymers were purchased from Polymer Source and were used without further purification. GPTMS (98%, Sigma-Aldrich) and glycidyl methacrylate (97%, Sigma-Aldrich) were used as surface energy-modifying agents. NMP (99%, Sigma-Aldrich) and DMF (anhydrous, Sigma-Aldrich) were used to dissolve the BCPs, and ethanol (99.9%, Samchun Pure Chemical Co. Ltd.) was used as the nonsolvent.

Synthesis of GPTMS-substituted BCPs (PS-*b*-G-PVP)

PS-*b*-PVP solution [2 wt %; solvent: NMP/DMF, 80:20 (w/w)] was reacted with GPTMS at 120°C, generating a new cyclic amide-bearing compound. The reaction time was varied from 0 to 120 min. The resulting PS-*b*-G-PVP solution was cooled to room temperature and used for membrane fabrication without any further purification.

Fabrication of copolymer membranes with hierarchical multiscale pores

The PS-*b*-G-P4VP solution was cast on a copper foil using a doctor blade and then placed in a convection oven at 110°C for 1 min to quickly remove the solvent. Subsequently, the incompletely dried BCP mixture was immersed in a coagulation bath containing ethanol (as a non-

solvent) for 1 hour at room temperature, leading to a porous solid-state film via the NIPS process. During the immersion process, unreacted GPTMS molecules were removed. Finally, oxygen plasma treatment (Femto Plasma Cleaner, 100 W) was carried out to remove dense layers on both the top and bottom surfaces and to transform the organic Si-containing G-P4VP blocks into inorganic silica layers, which contribute to the chemical resistance as well as the thermal stability of the resulting HMH-BCP membranes. As a control experiment, pure PS-*b*-P4VP copolymer thin films on silicon wafer were solvent-annealed in chloroform vapor at room temperature for 3 hours. Subsequently, the solvent-annealed films were characterized by atomic force microscopy (AFM) (fig. S15).

Characterization of HMH-BCP membranes

Surface and cross-sectional morphologies of HMH-BCP membranes were characterized by field emission SEM (Hitachi). For transmission electron microscopy (TEM) measurements, diluted copolymer solutions were cast on a Formvar-coated copper grid and subsequently immersed in a coagulation bath containing ethanol. The membranes were sectioned to a nominal thickness of 50 to 70 nm using a PT-PC PowerTome Ultramicrotome (RMC Products). The microtomed samples were characterized without staining treatment using TEM (JEOL, JEM-2100) in the bright-field mode. The STEM images, EDS spectra, and elemental mapping data were taken in the HAADF mode (JEOL, JEM-2100F) operating at an acceleration voltage of 200 kV. ^1H Nuclear magnetic resonance spectra (d_6 -DMSO) were acquired on a Varian UnityINOVA 600 (600 MHz) spectrometer. The attenuated total reflectance–Fourier transform infrared (ATR-FTIR) spectra of the membranes were recorded in reflectance mode using a Varian 670-IR spectrometer with a spectral resolution of 4 cm^{-1} under a nitrogen atmosphere. Negative-ion TOF-SIMS analysis was performed on a TOF-SIMS 5 (ION-TOF GmbH) equipped with Bi^+ and Cs^+ primary ion beam sources. The TOF-SIMS depth profiles were obtained in the dual-beam mode using a Bi^+ ion source for collecting spectra and a Cs^+ ion source for sputtering. A pulsed 25-keV Bi^+ beam was used as an analysis source at a target current of 1.3 pA. A 0.25-keV Cs^+ ion source, used as the sputter gun, bombarded the film surface at an incident angle of 45° to the surface at a target current of 35.0 nA. For water contact angle measurements, PS-*b*-G-P4VP thin films obtained after different GPTMS reaction times were fabricated on silicon wafers using 1 wt % polymer solutions by spin-coating at 3000 rpm for 2 min at room temperature. After drying at 70°C for 24 hours in a vacuum, the water contact angle was measured using a drop shape analyzer (DSA-100, KRÜSS GmbH). The pore size distribution of the HMH-BCP membrane was measured using mercury intrusion porosimetry (AutoPore IV 9500, Micromeritics Instrument Corp.).

Cell fabrication and electrochemical analysis as battery separator membranes

A coin cell (2032-type) was assembled by sandwiching a separator between a LiMn_2O_4 cathode [LiMn_2O_4 (Umicore)/carbon black/polyvinylidene difluoride (PVDF) binder, 92:3:5 (w/w/w)] and a $\text{Li}_4\text{Ti}_5\text{O}_{12}$ anode [$\text{Li}_4\text{Ti}_5\text{O}_{12}$ (Süd-Chemie)/carbon black/PVDF binder, 88:2:10 (w/w/w)], followed by filling with liquid electrolyte [1 M LiPF_6 in EC/PC (1:1, v/v, Soulbrain)]. The mass loadings of the cathode and anode were 24.5 and 18.5 mg cm^{-2} , respectively. All cells were assembled in an argon-filled glove box. The cell performance was investigated using a cycle tester (PNE Solution) under various charge/discharge conditions. The GITT was carried out using a potentiostat/galvanostat (VSP Classic, Bio-Logic) at a pulse of 2.55 mA cm^{-2} (=1.0 C) for 12 min, with a 60-min interruption

between each pulse. The structural variation of the membrane surface during charge/discharge cycling was investigated by TOF-SIMS with a Bi⁺ gun (25 keV, 1.02 pA) as a primary beam and with an O²⁺ gun (2 keV, 426.8 nA) as a sputter gun. As a control separator sample, a commercial PP/PE/PP separator (thickness, 20 μm; Celgard) was chosen. The PP/PE/PP separator was subjected to sulfonation treatment before cell assembly to overcome its poor wettability toward the polar liquid electrolyte.

SUPPLEMENTARY MATERIALS

Supplementary material for this article is available at <http://advances.sciencemag.org/cgi/content/full/1/6/e1500101/DC1>

Materials and Methods

Fig. S1. FTIR spectra of PS-b-P4VP and PS-b-G-P4VP films.

Fig. S2. Surface morphologies of top and bottom surfaces of the HMH-BCP membrane.

Fig. S3. Quantitative analysis of pore size distribution of the HMH-BCP membrane (GPTMS substitution reaction at 120°C for 30 min) using mercury intrusion porosimetry.

Fig. S4. Structural characterization of the microtomed HMH-BCP membrane (GPTMS substitution reaction at 120°C for 30 min).

Fig. S5. TOF-SIMS data of bare PS-b-P4VP and HMH-BCP membranes.

Fig. S6. Cross-sectional SEM images of a bare PS-b-P4VP membrane showing a sponge-like structure.

Fig. S7. Structural characterization of the PS-b-G-P2VP membrane.

Fig. S8. Structural characterization of the HMH-BCP (PS-b-G-P2VP) membrane (GPTMS substitution reaction at 120°C for 6 hours).

Fig. S9. Cross-sectional SEM images of PS-b-G-P4VP membranes (GPTMS substitution reaction at 120°C for 20 min).

Fig. S10. A conceptual ternary phase diagram of PS-b-G-P4VP membranes as a function of GPTMS substitution time.

Fig. S11. Cross-sectional SEM images of PS-b-G-P4VP membranes fabricated from ethanol and water nonsolvents.

Fig. S12. Characterization of PS-b-G-P4VP membranes fabricated as a function of drying time at 110°C.

Fig. S13. Characterization of internal cell resistance of HMH-BCP membrane and PP/PE/PP separator.

Fig. S14. Structural analysis of separator membranes after cycling test (200 cycles at charge/discharge current density of 1 C/1 C) at high temperature (50°C).

Fig. S15. Height mode AFM image of pure PS-b-P4VP copolymer thin films annealed in chloroform vapor.

References (34–37)

REFERENCES AND NOTES

- D. L. Gin, R. D. Noble, Designing the next generation of chemical separation membranes. *Science* **332**, 674–676 (2011).
- B. E. Logan, M. Elimelech, Membrane-based processes for sustainable power generation using water. *Nature* **488**, 313–319 (2012).
- Y. Y. Li, F. Cunin, J. R. Link, T. Gao, R. E. Betts, S. H. Reiver, V. Chin, S. N. Bhatia, M. J. Sailor, Polymer replicas of photonic porous silicon for sensing and drug delivery applications. *Science* **299**, 2045–2047 (2003).
- M. A. Shannon, P. W. Bohn, M. Elimelech, J. G. Georgiadis, B. J. Mariñas, A. M. Mayes, Science and technology for water purification in the coming decades. *Nature* **452**, 301–310 (2008).
- Y. La, C. Park, T. J. Shin, S. H. Joo, S. Kang, K. T. Kim, Colloidal inverse bicontinuous cubic membranes of block copolymers with tunable surface functional groups. *Nat. Chem.* **6**, 534–541 (2014).
- M. C. Orillall, U. Wiesner, Block copolymer based composition and morphology control in nanostructured hybrid materials for energy conversion and storage: Solar cells, batteries, and fuel cells. *Chem. Soc. Rev.* **40**, 520–535 (2011).
- C. R. Martin, Nanomaterials: A membrane-based synthetic approach. *Science* **266**, 1961–1966 (1994).
- J. H. Kim, J. H. Kim, K. H. Choi, H. K. Yu, J. H. Kim, J. S. Lee, S. Y. Lee, Inverse opal-inspired, nanoscaffold battery separators: A new membrane opportunity for high-performance energy storage systems. *Nano Lett.* **14**, 4438–4448 (2014).
- G. R. Guillen, Y. Pan, M. Li, E. M. V. Hoek, Preparation and characterization of membranes formed by nonsolvent induced phase separation: A review. *Ind. Eng. Chem. Res.* **50**, 3798–3817 (2011).
- S. Park, D. H. Lee, J. Xu, B. Kim, S. W. Hong, U. Jeong, T. Xu, T. P. Russell, Macroscopic 10-terabit-per-square-inch arrays from block copolymers with lateral order. *Science* **323**, 1030–1033 (2009).
- H. Yoo, J. I. Lee, H. Kim, J. P. Lee, J. Cho, S. Park, Helical silicon/silicon oxide core-shell anodes grown onto the surface of bulk silicon. *Nano Lett.* **11**, 4324–4328 (2011).
- D. Chen, S. Park, J. T. Chen, E. Redston, T. P. Russell, A simple route for the preparation of mesoporous nanostructures using block copolymers. *ACS Nano* **3**, 2827–2833 (2009).
- K. V. Peinemann, V. Abetz, P. F. Simon, Asymmetric superstructure formed in a block copolymer via phase separation. *Nat. Mater.* **6**, 992–996 (2007).
- H.-C. Kim, S.-M. Park, W. D. Hinsberg, Block copolymer based nanostructures: Materials, processes, and applications to electronics. *Chem. Rev.* **110**, 146–177 (2009).
- B. H. Jones, T. P. Lodge, Hierarchically structured materials from block polymer confinement within bicontinuous microemulsion-derived nanoporous polyethylene. *ACS Nano* **5**, 8914–8927 (2011).
- R. M. Dorin, H. Sai, U. Wiesner, Hierarchically porous materials from block copolymers. *Chem. Mater.* **26**, 339–347 (2014).
- R. Takekoh, T. P. Russell, Multi-length scale porous polymers. *Adv. Funct. Mater.* **24**, 1483–1489 (2014).
- D. T. Wong, S. A. Mullin, V. S. Battaglia, N. P. Balsara, Relationship between morphology and conductivity of block-copolymer based battery separators. *J. Membr. Sci.* **394**, 175–183 (2012).
- S. P. Nunes, A. R. Behzad, B. Hooghan, R. Sougrat, M. Karunakaran, N. Pradeep, U. Vainio, K. V. Peinemann, Switchable pH-responsive polymeric membranes prepared via block copolymer micelle assembly. *ACS Nano* **5**, 3516–3522 (2011).
- W. A. Phillip, R. M. Dorin, J. Werner, E. M. Hoek, U. Wiesner, M. Elimelech, Tuning structure and properties of graded triblock terpolymer-based mesoporous and hybrid films. *Nano Lett.* **11**, 2892–2900 (2011).
- Y. Sakatani, Boissière, C., Grosso, D., Nicole, L., Soler-Illia, G., Sanchez, C., Coupling nano-building block and breath figures approaches for the deigned construction of hierarchically template porous materials and membranes. *Chem. Mater.* **20**, 1049–1056 (2007).
- Y. Wang, C. He, W. Xing, F. Li, L. Tong, Z. Chen, X. Liao, M. Steinhart, Nanoporous metal membranes with bicontinuous morphology from recyclable block-copolymer templates. *Adv. Mater.* **22**, 2068–2072 (2010).
- S. Rangou, K. Buhr, V. Filiz, J. I. Clodt, B. Lademann, J. Hahn, A. Jung, V. Abetz, Self-organized isoporous membranes with tailored pore sizes. *J. Membr. Sci.* **451**, 266–275 (2014).
- M. Radjabian, V. Abetz, Tailored pore sizes in integral asymmetric membranes formed by blends of block copolymers. *Adv. Mater.* **27**, 352–355 (2015).
- V. Abetz, Isoporous block copolymer membranes. *Macromol. Rapid Commun.* **36**, 10–22 (2015).
- G. Xue, H. Ishida, J. Koenig, An investigation of the polymerization of pyridine with epoxy compounds. *Polymer* **27**, 1134–1137 (1986).
- N. Suzuki, H. Ishida, Effect of the miscibility between a silane and a sizing agent on silanol condensation. *J. Appl. Polym. Sci.* **87**, 589–598 (2003).
- J.-M. Tarascon, M. Armand, Issues and challenges facing rechargeable lithium batteries. *Nature* **414**, 359–367 (2001).
- O. K. Park, Y. Cho, S. Lee, H.-C. Yoo, H.-K. Song, J. Cho, Who will drive electric vehicles, olive or spinel? *Energy Environ. Sci.* **4**, 1621–1633 (2011).
- C. Zhan, J. Lu, A. Jeremy Kropf, T. Wu, A. N. Jansen, Y. K. Sun, X. Qiu, K. Amine, Mn(II) deposition on anodes and its effects on capacity fade in spinel lithium manganate-carbon systems. *Nat. Commun.* **4**, 2437 (2013).
- K. Xu, Nonaqueous liquid electrolytes for lithium-based rechargeable batteries. *Chem. Rev.* **104**, 4303–4417 (2004).
- E. F. Scriven, R. Murugan, *Pyridine and Pyridine Derivatives*, vol. 20 of *Kirk-Othmer Encyclopedia of Chemical Technology* (Wiley, Hoboken, NJ, ed. 4, 2005).
- T. Yim, H.-J. Ha, M.-S. Park, K. J. Kim, J.-S. Yu, Y.-J. Kim, A facile method for construction of a functionalized multi-layered separator to enhance cycle performance of lithium manganese oxide. *RSC Adv.* **3**, 25657–25661 (2013).
- S. Park, B. Kim, J.-Y. Wang, T. P. Russell, Fabrication of highly ordered silicon oxide dots and stripes from block copolymer thin films. *Adv. Mater.* **20**, 681–685 (2008).
- A. S. Zalusky, R. Olayo-Valles, J. H. Wolf, M. A. Hillmyer, Ordered nanoporous polymers from polystyrene-poly lactide block copolymers. *J. Am. Chem. Soc.* **124**, 12761–12773 (2002).
- N. Zhou, F. S. Bates, T. P. Lodge, Mesoporous membrane template by a polymeric bicontinuous microemulsion. *Nano Lett.* **6**, 2354–2357 (2006).
- Z. Wang, X. Yao, Y. Wang, Swelling-induced mesoporous block copolymer membranes with intrinsically active surfaces for size-selective separation. *J. Mater. Chem.* **22**, 20542–20548 (2012).

Acknowledgments: We thank members of the UNIST Central Research Facility for their support in analyzing structures of porous polymer membranes. **Funding:** This work was supported by the IT R&D program of the Ministry of Trade, Industry and Energy/Korea Evaluation Institute of Industrial Technology (MOTIE/KEIT; 10046309) and the Basic Science Research Program through the National Research Foundation of Korea funded by the Ministry of Science, ICT, and future Planning (2015R1A2A1A01003474). **Author contributions:** S.Y. and J.-H.K. contributed to fabricating the samples and conducted data analysis of all kinds: electrochemical test, SEM, TEM, X-ray diffraction, and FT-IR. M.S., H.P., and J.-H.K. assisted with membrane fabrication and characterization. S.P. and S.-Y.L. proposed and guided the research project. All authors contributed to writing the paper. **Competing interests:** The authors declare that they have no competing interests.

Submitted 12 February 2015

Accepted 1 June 2015

Published 24 July 2015

10.1126/sciadv.1500101

Citation: S. Yoo, J.-H. Kim, M. Shin, H. Park, J.-H. Kim, S.-Y. Lee, S. Park, Hierarchical multiscale hyperporous block copolymer membranes via tunable dual-phase separation. *Sci. Adv.* **1**, e1500101 (2015).